2016

Thermal and Mechanical Modeling of Metal Foams for Thermal Interface Applications

N. Trifale
Purdue University

E. Nauman
Purdue University

K Yazawa
Purdue University

Follow this and additional works at: http://docs.lib.purdue.edu/coolingpubs

Thermal and Mechanical Modeling of Metal Foams for Thermal Interface Application

Ninad Trifale
Mem. ASME
School of Mechanical Engineering,
Purdue University,
585 Purdue Mall,
West Lafayette, IN 47907
e-mail: ntrifale@purdue.edu

Eric Nauman
Mem. ASME
School of Mechanical Engineering,
Purdue University,
585 Purdue Mall,
West Lafayette, IN 47907
e-mail: enauman@purdue.edu

Kazuaki Yazawa
Mem. ASME
Birck Nanotechnology Center,
Purdue University,
585 Purdue Mall,
West Lafayette, IN 47907
e-mail: kyazawa@purdue.edu

We present a study on the apparent thermal resistance of metal foams as a thermal interface in electronics cooling applications. Metal foams are considered beneficial for several applications due to its significantly large surface area for a given volume. Porous heat sinks made of aluminum foam have been well studied in the past. It is not only cost effective due to the unique production process but also appealing for the theoretical modeling study to determine the performance. Instead of allowing the refrigerant flow through the open cell porous medium, we instead consider the foam as a thermal conductive network for thermal interfaces. The porous structure of metal foams is moderately compliant providing a good contact and a lower thermal resistance. We consider foam filled with stagnant air. The major heat transport is through the metal struts connecting the two interfaces with high thermally conductive paths. We study the effect of both porosity and pore density on the observed thermal resistance. Lower porosity and lower pore density yield smaller bulk thermal resistance but also make the metal foam stiffer. To understand this tradeoff and find the optimum, we developed analytic models to predict intrinsic thermal resistance as well as the contact thermal resistance based on microdeformation at the contact surfaces. The variants of these geometries are also analyzed to achieve an optimum design corresponding to maximum compliance. Experiments are carried out in accordance with ASTM D5470 standard. A thermal resistance between the range 17 and 5 $K\,cm^2/W$ is observed for a 0.125 in. thick foam sample tested over a pressure range of 1–3 MPa. The results verify the calculation based on the model consisting the intrinsic thermal conductivity and the correlation of constriction resistance to the actual area of contact. The area of contact is evaluated analytically as a function of pore size (5–40 PPI), porosity (0.88–0.95), orientation of struts, and the cut plane location of idealized tetrakaidecahedron (TKDH) structure. The model is developed based on assumptions of elastic deformations and TKDH structures which are applicable in the high porosity range of 0.85–0.95. An optimum value of porosity for minimizing the overall interface thermal resistance was determined with the model and experimentally validated. [DOI: 10.1115/1.4032957]

1 Introduction

Metal foams have been receiving considerable attention over the years for mechanical applications such as energy absorption, damping, etc. Its low density, large area moment of inertia, and high specific strength make it a more than a viable option for such applications. Lately there has been significant research for use of porous materials for thermal management applications as well. The large surface area-to-volume ratio, lower elastic modulus, and relatively higher thermal conductivity ($\sim$10 W/m K) [1,2] make metal porous structures suitable for heat dissipation applications such as heat sinks [1] and thermal interface materials (TIMs). The TIMs are used to reduce the contact resistance between two opposing surfaces, typically between the chip and heat spreader or heat spreader and heat sink.

Prasher [3] give a detailed review of the state-of-the-art thermal interfaces currently available. Thermal greases, gels, and phase change materials have an excellent thermal performance with resistance of the order of 0.26 K cm²/W. Carbon-based porous structures such as high conductivity carbon foams (150 W/m K) [4], 3D graphene networks [5], and ultrathin graphite foams [6] have been shown to be promising materials for high-performance TIM.

The works on the carbon-based porous structures provide motivation for the current study for analysis of metal foams for low heat flux applications.

The design objective for an ideal TIM is low thermal resistance with high compliance. The total thermal resistance is a combined effect of the intrinsic thermal resistance through the medium and the contact resistances on the contacting surfaces. The contact resistance for two materials depends on the actual area of contact which depends on the applied pressure and correlated through the compliance. Larger mechanical compliance is thus desirable and can improve performance as a TIM. Additionally, the metal foams can incorporate various gels and thermal greases within the voids, which can enhance the effective thermal conductivity as well as reduce the contact resistance. We do not investigate this addition in the present study and is a part of a larger study (Fig. 1).

The effective thermal conductivity of the metal foams is obviously lower than that of the bulk solid. However, the objective is to obtain a competitive thermal resistance compared to the current state-of-the-art TIMs in market such as "self-sustain" gels, thermal greases, or thermal pads. This study aims at combining advantages of metal pads and thermal greases. The metal foam provides continuous pathways like "highways" for heat flow between the two boundary contact surfaces unlike thermal greases but are also more compliant than thermal pads.

Krishnan et al. [7] have carried out comprehensive simulation of transport through foams by a considering a body cubic center
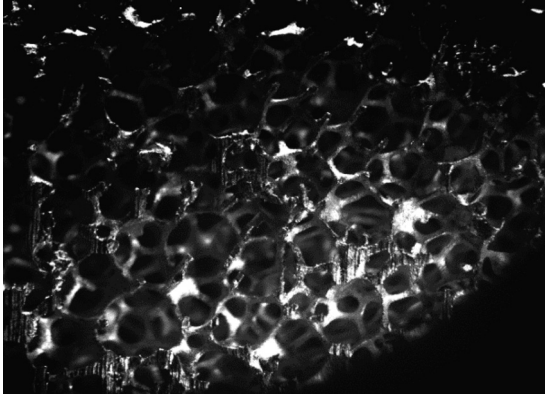
Fig. 1 Foam sample used for experimentation, 10PPI 0.93 porosity

Fig. 3 Schematic representation of different components of total thermal resistance

(BCC) model for predicting effective thermal conductivity. Doermann and Sacadura [8] provide an efficient parallel–series model for conduction and have additionally incorporated the effect of radiation. Similar conduction modeling strategies have been used in the current study to predict the effective thermal conductivity of foams, and the results have been confirmed to be in general agreement with the experimental data and models presented in the literature.

The mechanical and thermal effective properties of the foams such as elastic modulus, yield stress, and thermal conductivity are functions of the geometric parameters, namely, pore size, pore density, and porosity. These geometric parameters are interdependent. Hence, the effective properties of the porous material are analyzed as a function of these geometric parameters, which are the key in engineering the best design by finding an appropriate combination of mechanical and thermal properties.

A tradeoff is observed between the intrinsic thermal resistance and the contact resistance. The effective thermal conductivity is higher for lower porosity since more metal will intuitively result in larger conductivity but also lesser compliance. The contact resistance accordingly decreases with increasing porosity up to a point beyond which it increases exponentially for 100% porosity. Analogous to this, the contact area is shown to have a maximum value for a specific combination of porosity and pore size as will be discussed later in the paper. Subsequently, the magnitude of relative contributions of both the components, contact resistance and intrinsic resistance, to the total resistance is determined. The area of contact is analyzed by the deformation of the multiple struts in porous structure. Numerical simulations for the effective thermal conductivity are carried out by using a widely accepted model of TKDH unit cell (Fig. 2).
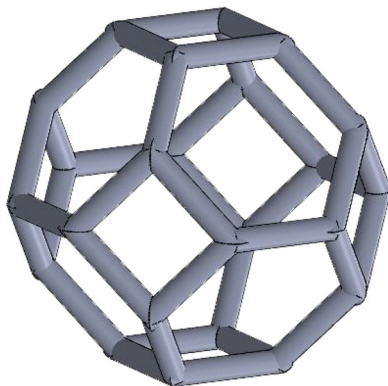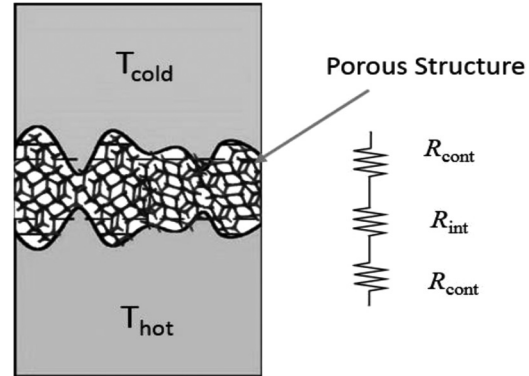
2 Methodology

Figure 3 shows the macroscopic model of a generic thermal interface. We split the analysis of the total thermal resistance into two sections: the intrinsic thermal resistance and the contact thermal resistance. The effective thermal conductivity of the foam material is going to influence the intrinsic resistance, whereas the deformation and area of contact are going to affect the contact resistance.

We focus the model on heat transfer through conduction by assuming that majority of the heat is transferred through the mode of conduction as compared to that through natural convection and radiation. Studies have been conducted by Bauer et al. to show that radiation effects are dominant at high temperatures [9]. The current models and applications considered have operating temperatures much lower for radiation to be significant. Experiments for evaluating the total thermal resistance are carried out for multiple thickness samples so that the intrinsic and contact resistance components can be separated out. The models developed for predicting effective thermal conductivity and the contact resistance are then empirically correlated with the experimentally observed values. The experimentation details are discussed in Sec. 3.

3 Experimentation

The experimentation is carried out with a test setup complying with ASTM D 5470 (Fig. 4(*b*)). The schematic of the test setup is shown in Fig. 4(*a*). The setup has two cylindrical "flux meters" made of electrolytic iron, 2.54 cm in diameter. The test specimens are placed between the flux meters. The thermal conductivity of flux meter material is known as a function of temperature within 2% error. Four thermocouples (36 AWG T-type) are embedded within each of the flux meters in a center at exact spacing of 0.108 cm along the axial direction. NetDaq Fluke system was used for data acquisition. A heater source and a heat sink made of 2.54 cm diameter copper cylinder are placed on the top and the bottom of the column, respectively. The heat source has three cartridge heaters within, which are connected to a DC power source. Ethylene glycol, maintained at −10 °C, is circulated through the heat sink. The heat flow is assumed to be one-dimensional from the top of the column to the bottom. The heat source and heat sink are insulated by fiber glass wrapped with tape. Thermal grease is applied between the flux meter blocks and the heat source and heat sink contacts.

The test column is enclosed in cylindrical radiation shield to minimize the radiation losses. A pneumatic loading cylinder is located at the bottom of the column and controlled by a pressure regulator valve, while a load cell is mounted on top of the column. The heat flux is evaluated from the slope of best linear fit of four point temperatures based on the 1D thermal conduction assumption. The net heat flux across the test specimens is taken as average of the two fluxes from the two flux meters. The variance of
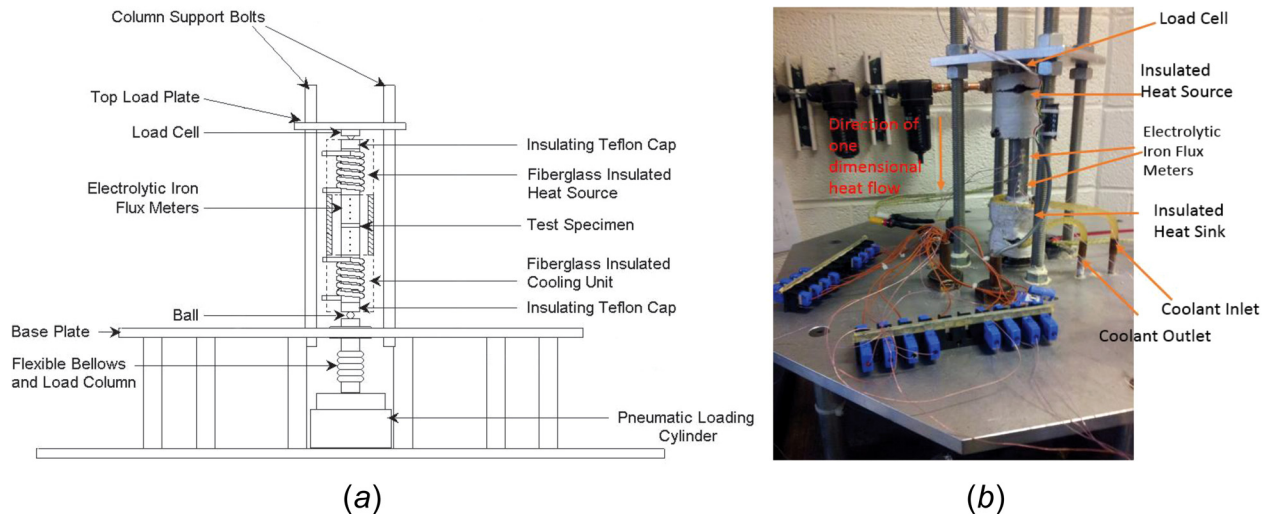

Fig. 2 TKDH structure with six squares and eight hexagons

Fig. 4 (*a*) Schematic representation of experimentation setup and (*b*) actual experimentation setup

Table 1 Various uncertainties associated with the experimental setup

Variable	Temperature (K)	Column diameter (cm)	Axial thermocouple location (cm)	Electrolytic iron thermal conductivity (%)	Column axial load (lbf)
Uncertainty	0.2	0.00254	0.0127	2	0.1

flux through the force meters was found out by evaluating the difference in the two fluxes relative to the average heat flux for all the experiments. The average variance for Q_1 and Q_2 was found to be about 5% of the average heat flux across the sample. The temperatures T_1 and T_2 at the surfaces of the sample are found by extrapolating from the four point temperatures in each flux meter column. The total thermal resistance is calculated as

$$Q_{avg} = \frac{Q_1 + Q_2}{2} \quad (1)$$

$$R_{tot} = \frac{T_1 - T_2}{Q_{avg}} \quad (2)$$

where T_1 and T_2 are the extrapolated temperatures at the surface of the sample.

The thermal resistance is calculated under steady-state conditions which are defined as condition wherein the temperature change is less than $0.50\,°C$ over 30 min time period. The total thermal resistance is characterized under various loads and for multiple thicknesses of the samples.

The power input at heat source and temperature at heat sink is adjusted such that the average temperature of the sample was roughly close to the atmospheric temperature. This was done to minimize the heat transferred through convection at the sample surface.

The total effective uncertainty of the overall thermal resistance is calculated based on the uncertainty of the individual measurements of temperatures, temperature gradients, dimensions of the parts, and material properties. It was found that the variation of the heat flux measured in the two flux meters was between 3% and 10% of the average heat flux calculated. The individual uncertainties for various variables are stated in Table 1.

The uncertainty varied with time throughout the experiment as well as with every sample tested. This variation with respect to was due to the changing uncertainty in temperature extrapolation at every instant. The overall average uncertainty for the experiments carried out across all samples was found to be 15% of the measured thermal resistance value.

3.1 Effect of Porosity and Pore Size. The experimentation was carried out for three different thicknesses—0.125 in. (3.175 mm), 0.25 in. (6.35 mm), and 0.5 in. (12.7 mm). All three samples were tested for three different porosities 0.87, 0.93, and 0.95 as well as four different pore sizes—5 PPI, 10 PPI, 20 PPI, and 40 PPI. PPI stands for pores per inch following the industry standard. This PPI is a measure of the pore size, e.g., 10 PPI is equivalent to about 2 mm. The samples were made of aluminum foam consisting of 6101 T6 alloy and were manufactured by ERG Aerospace Company.

3.2 Evaluation of Effective Thermal Conductivity and Contact Resistance. It is possible to evaluate the thermal conductivity of the samples if multiple thickness samples are tested for thermal resistance (refer Eq. (3)). The total thermal resistance is a sum of the intrinsic resistance (given by t/k) and the contact resistance as expressed in Eq. (18). The effective thermal conductivity and contact resistance were evaluated by solving the three equations corresponding to three different thicknesses for which the total thermal resistance was measured. The contact resistance was assumed to be independent of thickness of the sample. The effective conductivity measurements are carried out for the smallest load so as to minimize the effect of deformation on the measured effective conductivity

$$R_{tot} = \frac{t}{k_{eff}} + 2R_{cont} \quad (3)$$

The contact resistance is found as a continuous function with respect to pressure by interpolating from the measured pressure points.

4 Intrinsic Resistance Model

The intrinsic resistance of the TIM is determined using the models developed for the effective intrinsic thermal conductivity. The bulk resistance is calculated using the thickness and total area of the samples used for experimentation

$$R_{\text{int}} = \frac{t}{A_t \times k_{\text{eff}}} \qquad (4)$$

The effective thermal conductivity varies with porosity and not with pore size; as a result, the intrinsic resistance is solely dependent on the porosity of the sample [10]. The effective thermal conductivity has been evaluated numerically and compared with the experimental data [1] and analytic models [10,11] in the literature.

There are various approaches to analytically determine the effective thermal conductivity. Most of the approaches differ in the choice of representative volume element. Paek et al. [12] analyzed the effective thermal conductivity considering a simple cubic structure unit cell with orthogonal struts for a preliminary prediction. As an extension, a fraction of material struts is considered along and perpendicular to the heat flow direction, and the conductivity is evaluated as a weighted sum [13]. Leong and Li [14] have developed a rectangular shell model with quarter-spherical pockets at the vertices, and the model is further subdivided into multiple layers and the conductivity of the layers is evaluated separately. There are also statistical approaches [15] as well which result in similar predictions to that of the cubic model. The radiation effect is found to be an important factor to be considered for further improving the prediction but only at very high temperatures [9].

Boomsma and Poulikakos [10] have proposed a geometrical model, repeating TKDH cell structure. The geometry is approximated by cubes at the nodes and cylinders as the struts for the TKDH. Owing to the symmetry, 1/16th part of the TKDH is used to evaluate for four different sublayers. The general rule of mixture states that heat conducted in the metal struts and stagnant fluid in the vacant space are proportional to their volume fractions, i.e.,

$$k_{\text{eff}} = \varepsilon \times k_f + (1 - \varepsilon) \times k_s \qquad (5)$$

where k_{eff} is the effective thermal conductivity, k_s is the solid thermal conductivity, and k_f is the fluid thermal conductivity. The same model has been extended in Ref. [11] to incorporate the effect of the orientation of the struts. This formulation in not directly applicable in the current study, and the orientation of the struts needs to be accounted for.

Bauer [9] used further comprehensive approach to evaluate the effective thermal conductivity, by considering perturbations in the continuous medium with a governing differential equation as continuum instead of analyzing a representative volume element. They found that the ratio of effective thermal conductivity to the bulk solid is directly proportional to the relative density raised to $1/n$th power, where the value of n is a semi-empirical constant. In most of the above literature, the medium is assumed to be homogenous and rule of mixtures applied to a representative volume element. Furthermore, for parallel conduction in metal and fluid, the ratio of heat conducted through each path is proportional to the volume fraction. This coupled with the approximation that the temperature at one layer is constant, in solid as well as fluid, reduces the problem to 1D conduction.

Additionally, almost all the existing models do not take into account the heterogeneousness, density gradients, and anisotropy caused by manufacturing process. Natural convection and radiation are also neglected in most of the studies, because of relatively minor contributions. We make the same assumptions in this study as it is supported by thorough experimentation in literature [16].

4.1 Numerical Simulation. In this section, we present a numerical study on the effective thermal conductivity. Druma et al. [17] have carried out finite element method-based simulations for heat conduction in array of carbon foam and compared to analytical model developed in literature [7]. Maruyama et al. [18] generated 3D images of carbon structures, and subsequently, the same model is used for finite element simulations for heat conduction on the "scanned" model. This representative volume element for metal foams is simply transformed to numerical simulations for porous structure. We use a similar approach to the above studies but by considering a TKDH unit cell as representative volume element instead.

The TKDH approximation serves as a simple approximation for not only evaluating the thermal conductivity but also for modeling the geometry at surface and characterizing elastic deformation at struts to analyze the contact area. We choose the TKDH for the current study to maintain consistency across the mechanical and thermal characterizations. We compare the numerical simulation results with the analytic models developed by Boomsma and Poulikakos [10] and Dai et al. [11]. We also present another simplified model which provides good prediction for the effective thermal conductivity. The latter model assumes the thermal resistance network of struts in the TKDH structure to find one effective resistance.

In this study, a symmetrical unit cell generated by a BCC distribution of voids represents a unit volume for the thermal conductivity in porous structure. We assume that the properties of the entire structure are depicted by the unit cell. We generated the geometry for the FEM model by subtracting overlapping part of nine contributed spherical volumes from a cube. The dimensions of the cube are equivalent to the size of the unit cell. Due to the BCC structure, the sphere centers are located at the eight vertices and the center of the cube. We define a dimensionless parameter $p = r/a$, where "r" is the radius of the sphere void and "a" is the cube edge length.

Porosity as a function of p is evaluated by the volumes of the spheres and the intersection of the volumes. The expression of porosity ε is given by [7]

$$\varepsilon = \frac{2\left(\frac{4\pi}{3}r^3\right) - \frac{\pi}{3}(4r+s)(2r-s)^2 - 2\pi\left(r-\frac{a}{2}\right)^2\left(2r+\frac{a}{2}\right)}{a^3} \qquad (6)$$

where s is the center to center distance between the inline spheres. The foam will be open cell if

$$r > \sqrt{\left(3 \times \left(\frac{a}{2}\right)^2\right)} \qquad (7)$$

The effect of pore density and pore size is inherent in the ratio "p" which defines the porosity. Eighteen different geometries were considered, varying the geometry ratio by varying radius of sphere voids and keeping cube size constant. The investigated porosity varies from 0.825 to 0.996. These high porosity values are intentionally selected in order to investigate the mechanical compliance with a lower bound effective thermal conductivity.

If the structure is approximated as a TKDH, there will be obviously more mass at the nodes as compared with struts in the model. For such a case, the assumption made by Boomsma and Poulikakos [10] and Dai et al. [11], i.e., cubes as nodes and cylinders as the struts for the TKDH, can account for this varied distribution.

(i) Boundary conditions and material properties:
The model shown in Fig. 5 was used as geometry for the analysis. A constant temperature difference was applied across the interface. The thermal conductivity is assumed to be temperature independent. Aluminum thermal conductivity value 175 W/m K was applied to the metal part to compare with experiments. Symmetry condition was imposed for the remaining four faces of the whole thermal interface volume.

(ii) Control of the FEM calculation:
Steady-state thermal response is calculated using ANSYS solver for 18 different porosities with varying p.
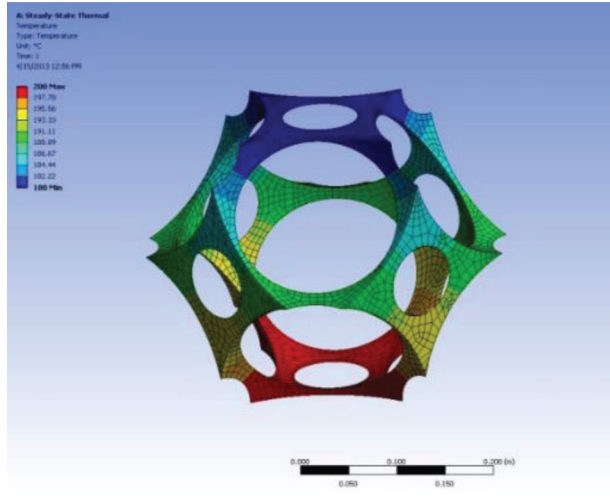
Fig. 5   Temperature distribution for 0.9 porosity unit cell

Heat transfer by convection and radiation was neglected. A fine mesh was used for the setup. A hex-dominant mixed mesh including "Solid87" (ten-node tetrahedral) and "Solid90" (20-node hex element) was used. Number of nodes varied from 13,847 to 90,497 and the elements from 4153 to 29,068, depending on the geometry (porosity) in question.

(iii) Effective flux and effective thermal conductivity:
The heat flux was evaluated at the center plane of the geometry perpendicular to conduction direction, and the total heat flow was calculated by multiplying the flux by the area of the section. Average value of the heat flux was considered as the distribution of the heat flux across the plane is nonuniform. The effective flux was then evaluated for the apparent area of contact. The effective thermal conductivity was calculated for all the geometries using Fourier's law.

4.2   Resistance Network Analogy. A TKDH structure is considered as shown in Fig. 3. The 36 individual struts of the TKDH are modeled as individual resistances (Fig. 6). Such modeling strategies have been previously employed in literature [7] and serve a simple method to predict effective thermal conductivity of foams. The individual thermal resistance is L/kA_c, where L is the length of one strut, k_s is the thermal conductivity, and A_c is the cross section area of the strut. Twenty-four out of the 36 struts are shared between the adjoining unit cells. The struts lying in the horizontal planes will not contribute in the effective thermal
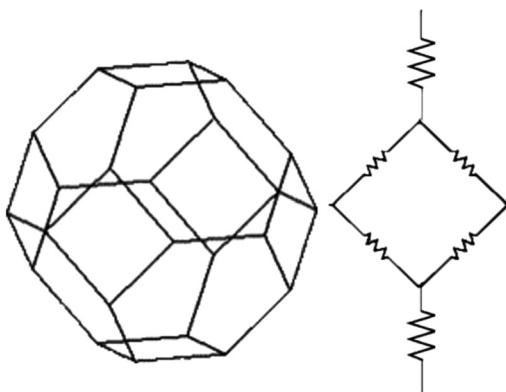

Fig. 6   Resistance network analogy, individual struts as part of resistance network

resistance. Using these properties, the cell-based effective resistance is evaluated with the thermal resistance network.

The length and the cross section area are determined by porosity and pore density specified by manufacturer (PPI)

$$1 - \varepsilon = \frac{24\pi r^2 L + 16\pi c r^2}{\left(\sqrt{8}L\right)^3} \tag{8}$$

where c is

$$c = \frac{R^3}{r^2} \tag{9}$$

$$L = \frac{0.0254 \times 3}{\text{PPI}\left(\sqrt{8}\right)} \tag{10}$$

where PPI is the pore density measured in unit pore per inch. Finally,

$$r = \sqrt{\frac{(1 - \varepsilon)\left(\sqrt{8}L\right)^3}{\pi(24L + 16c)}} \tag{11}$$

The porosity by definition is calculated by the solid volume occupied within the bound unit cell. The parameter "c" accounts for the volume occupied by the solid spheres at the nodes accounting for mass concentration. The parameter is evaluated using the empirical relation for "e" through works of Prasher [3]. Every individual resistance is given by

$$R_{\text{strut}} = \frac{L}{k_s \pi r^2} \tag{12}$$

Substituting these final expressions (Eqs. (8)–(12)), we get the effective thermal conductivity as

$$k_{\text{eff}} = \frac{k_s(1 - \varepsilon)}{3} \tag{13}$$

The effective resistance depends linearly on porosity, which is similar to results observed in other analytic models and simulation results presented in this study as will be discussed in Sec. 5.

4.3   Results for Effective Thermal Conductivity. The effective thermal conductivity of the foams was evaluated at porosities more than 0.8 using the numerical simulations and resistance network analogy model and compared with the experimental results from literature as well as experiments carried out as a part of this study. The various thermal conductivities were plotted against porosity (Fig. 7).

Figure 5 shows the temperature variation within the unit cell from the numerical simulation results at 0.9 porosity. The assumption of one-dimensional conduction is valid as shown in Fig. 5, wherein the parallel temperature gradient is observed along the conduction direction. The average heat flux was then considered for the cross section selected, in order to compensate for large variations of heat flux on the same plane. The thermal conductivity was calculated using Fourier's law.

As expected, the effective thermal conductivity reasonably drops as porosity increases toward unity. The trend is almost linear excluding very high porosity range (>0.97) for the simulation results. All the other models as well as experimental data suggest a linear behavior.

The two curves in Fig. 7 show the analytic models. The models need a parameter "e" to be calibrated against experimental data. The two curves correspond to $e = 0.198$ [4] and $e = 0.339$ [3]. The values of the parameters are the same as what the authors used it for the comparison with the experimental data in their literature. The analytic models provide upper and lower bounds to the
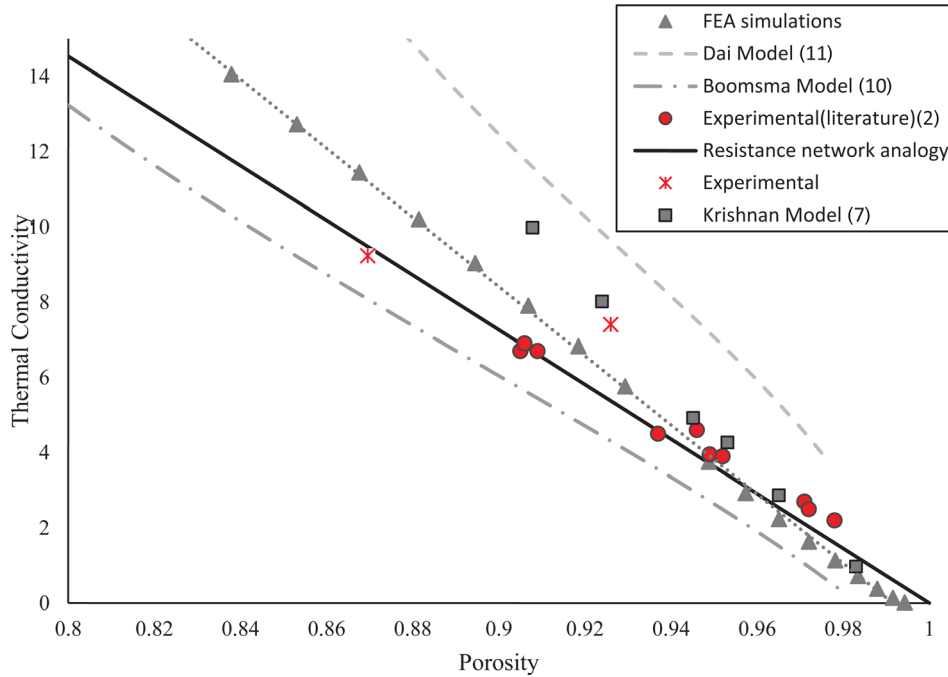
Fig. 7 Effective thermal conductivity, comparison of multiple methods

experimental data. The FEM simulation results are shown by circular symbols. The simulation results are very close to the values obtained from the experiments [1,2]. Simulation results are close to the BCC model provided by Krishnan et al. at higher porosities. This result is expected since similar geometry approximation has been used in both the cases. A best fit linear curve to the simulation results is also shown on the same plot. The standard deviation of 0.76 was observed for the experimental data about the best fit curve.

The resistance network analogy shows a linear trend as well but with a different slope. The resistance network analogy and the BCC model provided by Krishnan et al. [7] provide close predictions for the effective thermal conductivity at high porosity values. The predicted values of this model are much closer to the experimental data. Note that the validity of all of these models is for porosity values greater than 0.8 due to the open cell limit for TKDH approximation.

5 Contact Thermal Resistance

We developed an analytic model to connect the actual area of contact with the contact thermal resistance. The model allows us to analyze the deformation of a unit cell to evaluate the contact area as a function of porosity and pore size. The actual area is normalized by the apparent area of contact and correlated to the contact resistance. We use the model developed by Yovanovich et al. [19,20] for rectangle-on-rectangle contact. The constriction resistance is calculated for every strut and then all of them consolidated to predict the effective constriction resistance. The thermal resistance of a strut is given by

$$R_{\text{cont}} = \frac{\psi}{\sqrt{A_c} \times k_c} \qquad (14)$$

where ψ is the alleviation factor, which is determined from the area of contact normalized with respect to unit cell area

$$\psi = \frac{1}{\epsilon} = \frac{A_t}{A_{\text{cont}}} \qquad (15)$$

The thermal conductivity of contacting material is another contributor for the constriction thermal resistance. The conductivity of the electrolytic iron flux meters which are the adjoining materials in the sample is also considered to calculate the spreading resistance. A self-similarity model [21] could be used for analyzing the contact resistance if the pores are considered to be filled with fluid in which case the ratio of solid to fluid conductivity will have a substantial impact on the contact resistance. The contact thermal resistance is determined as function of porosity and pore size. Therefore, a combined total resistance is calculated from the geometry factor and the thermal conductivity.

5.1 Mechanical Deformation and Area of Contact. The actual area of contact was evaluated from the microdeformation model of the struts as follows. There has been substantial research for determining the mechanical properties of porous structures. Study carried out by Gibson and Ashby [22] consisted of extensive experimental coupled with analytical models to predict the effective Young's modulus and yield stress. A conclusion of the work was that the effective Young's modulus is directly proportional to the square of relative density $(1 - \varepsilon)$. Similar results have been observed by various authors though experimentation [22,23].

There are also several numerical studies. Wicklein and Thoma [24] have modeled a sample foam using an FEM software. The TKDH model is used to obtain stiffness matrix and evaluate the effective Young's modulus by Kwon et al. [23]. Zhu et al. [25] considered the TKDH model with force/moment balance at specific nodes/struts to analytically find Young's modulus as a function of the relative density. The results agree with the experimental data and the empirical relationships [22]. Sullivan et al. [26] included anisotropy in the model by considering elongated TKDH. Simone and Gibson [27] have considered only a 2D structure (honeycomb) and have analytical and numerically evaluated it. They have confirmed that the effective Young's modulus varies with respect to square of relative density. A similar relationship is observed for the yield stress whereas the Poisson's ratio does not change with respect to the relative density.

In the present study, the models developed in the literature, specifically by Zhu et al. [25] for TKDH unit cell, were used to determine the overall deformation. For determining surface deformation, we considered a homogeneous and repeating arrangement
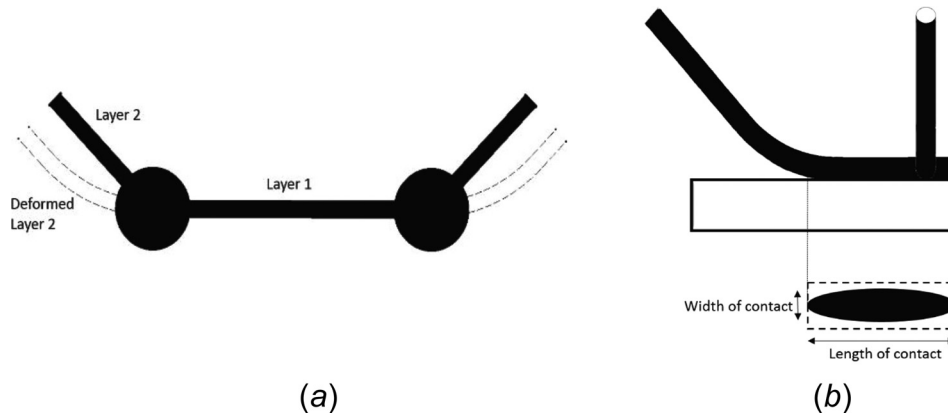
Fig. 8 (*a*) Bottom layer in contact initially, adjacent layer struts deform to come in contact with the surface and (*b*) contact area patch for struts

of TKDH cells. This geometry was chosen not only to maintain consistency but also because the porous structure resembles TKDH due to the nature of manufacturing process, where the minimal surface energy is preferred. TKDH has been shown to have minimum surface area out of all polyhedrons [28]. We assumed that the struts of the unit cell are cylinders with radius "*r*," and the nodes of the struts are considered as spheres depicting the nature of the porous structure. The diameter of the spheres is determined by empirical factor "*e*." A detail analysis for the above assumptions was provided by Boomsma and Poulikakos [10]. The deformation was evaluated for a unit cell and the normalized area was found out. The contact area of a cylinder on flat contact surface is a rectangle. Beam bending equations were used to calculate the length of strut coming in contact with the opposing surface. Strut radius and length were calculated from the porosity and pore size.

Initially, the struts in the layer closest to the opposing surface are the first to deform and come in contact followed by the adjacent layer (second layer) after further deformation (Fig. 8(*a*)). We analyze the individual contribution of the struts to the area of contact, considering two adjoining layers to surface. In addition, we extend the analysis for variation of the orientation angle of the struts. The Timoshenko's beam theory is used to evaluate the contact length of the contact area. The governing differential equation is given below:

$$EI\frac{\mathrm{d}^2v}{\mathrm{d}x^2} = M \qquad (16)$$

Analytic solution for distributed load on the beam is used to calculate the angle of deformation at every point on the beam. The point where the slope of deflection curve is equal to the original orientation angle of the strut gives the location of the initial contact. For the bottom layer, entire strut length is already in contact and the length of the contact is L. The width of the contact w is found using Hertz contact theory [29] for cylinder on flat configuration given by

$$w = \left(\frac{4Pr}{\pi E_s l_x}\right)^{1/2} \qquad (17)$$

We calculate an example case with a normalized area of contact for a 50 psi (344.74 kPa) loading pressure to match the experimental boundary conditions. The total area of contact is calculated for the bottom two layers: the first one is completely in contact and the other deforms to come in contact

$$A_{\mathrm{cont}} = \left(\frac{n}{2}\right) \times L_{\mathrm{contact}} \times w_2 + \left(\frac{n}{2}\right) \times L_{\mathrm{strut}} \times w_1 \qquad (18)$$

where subscript 2 refers to the deforming layer and subscript 1 refers to the layer already in contact.

5.2 Results for Area of Contact and Contact Resistance. The area of contact can be quantified through two parameters: the width of contact and the length of contact. These two factors have opposing trends. Since the radius of the strut decreases with increasing porosity, the deformation as well as length of contact increases, whereas the width of contact decreases with increasing porosity. Similar trend is observed for variation of PPI (inverse of pore size). The radius of the struts decreases with increasing PPI. Increasing PPI also decreases the strut length and reduces the total deformation, and hence decreases the length of contact. There is clearly a tradeoff between the width and length of contact. It is possible to find out an optimum value of porosity which results in maximum area. Figure 9(*a*) gives the normalized area of contact with respect to the porosity and the orientation angle of the second layer struts. Ideally, we can expect 45 deg angle for pure uniform and symmetric TKDH cells. This angle variation serves as a generalized model to incorporate any asymmetries within the geometry. The sharp peak in Fig. 10(*a*) for the width of contact corresponds to initiation of the contact of the second layer. When the second layer comes in contact, we observe a rapid and steady rise in the length of contact (Fig. 10(*b*)). It is observed that the maximum value of area of contact does not change with respect to the orientation angle, but the porosity corresponding to the maximum area of contact does change.

When the total load increases, the magnitude of the maximum area of contact does not change. However, the porosity value corresponding to the maximum area value decreases. Furthermore, it has been shown that the contact resistance is proportional to the inverse of square root of actual area of contact [20]. Figure 9(*b*) shows the variation of contact area index with respect to pressure and pores per inch. The comparison to the experimental result is discussed in Sec. 6. Figure 11 shows the variation of inverse of square root of area of contact with respect to pressure for various pore sizes. The trends observed are similar to the trends observed experimentally for the contact resistance as is discussed in Sec. 6.

5.3 Contact Resistance From Experiments. Contact thermal resistance was evaluated for the two sets of experiments for porosity and pore size. The best fit curve is shown in Fig. 12. A transition effect is observed in case of variation of PPI close to 0.5 MPa pressure, where at higher pressure, larger PPI actually results in lower resistance. In the case of porosity variation, a larger porosity results in a larger contact resistance. The continuous curves are obtained by interpolating the total thermal resistance from the measured data points (e.g., Fig. 19).
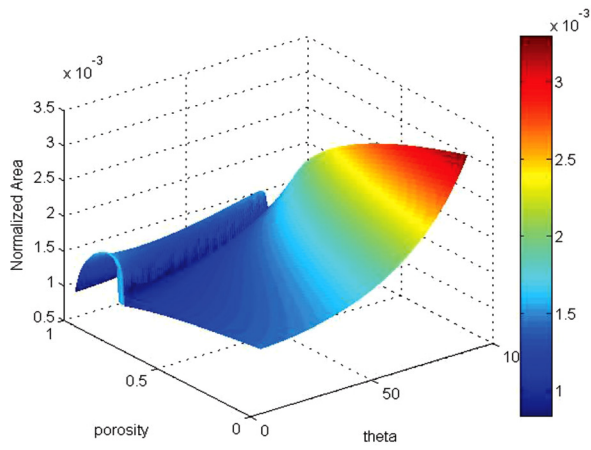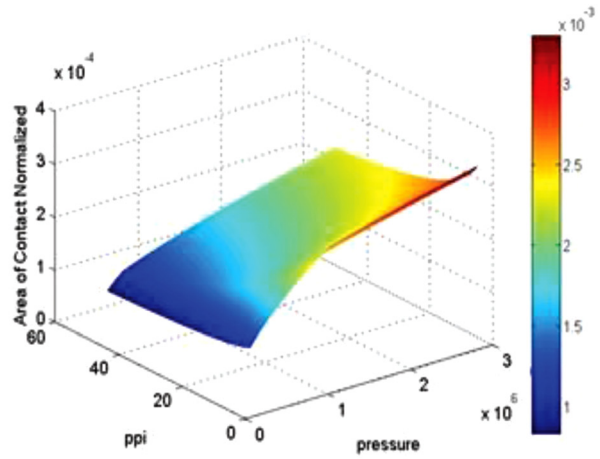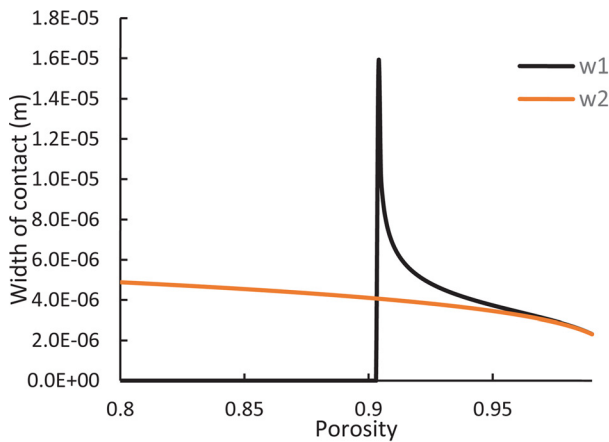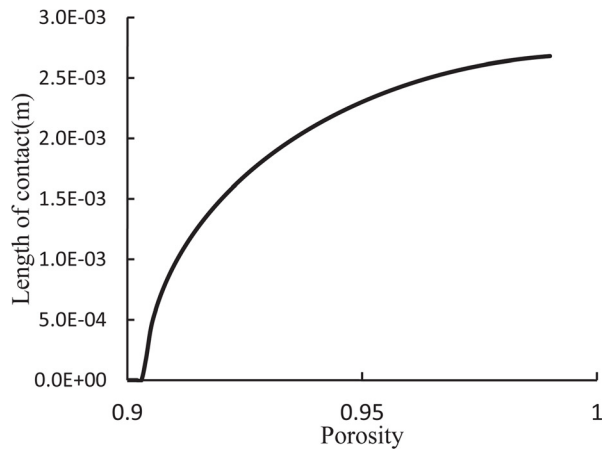
Fig. 9 (*a*) Normalized area against orientation angle and porosity and (*b*) normalized area of contact as a function of PPI and pressure

Fig. 10 (*a*) Width of contact patch for two layers sharp peak marks initiation of second layer contact and (*b*) length of contact patch for layer 2. The second layer deforms but only higher porosity foams have deformation large enough to make contact.
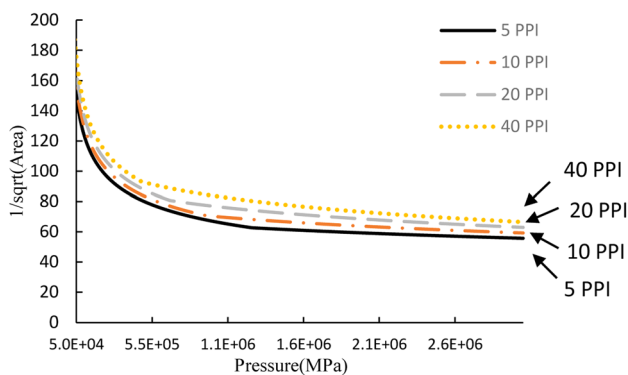

Fig. 11 Trends for $1/\sqrt{}$(area) against pressure—similar to the contact resistance trend

From total thermal resistance data for any two different thickness samples from this set, the contact resistance and thermal conductivity can be evaluated for a specific porosity and PPI. A best fit contact resistance value is found using the three set of equations to evaluate the two unknowns of thermal conductivity and contact resistance. The contact resistances are evaluated in each case by fitting curve as shown in Fig. 13. The thermal resistance value is extrapolated to the value crossing the "zero thickness." The contact resistance is dependent on both porosity as well as the applied load. As expected, the contact resistance decreases monotonically as the load increases.

6 Total Thermal Resistance

The model predictions for the intrinsic and contact resistance are consolidated and compared with the experimental data for the total thermal resistance with respect to porosity and pore size
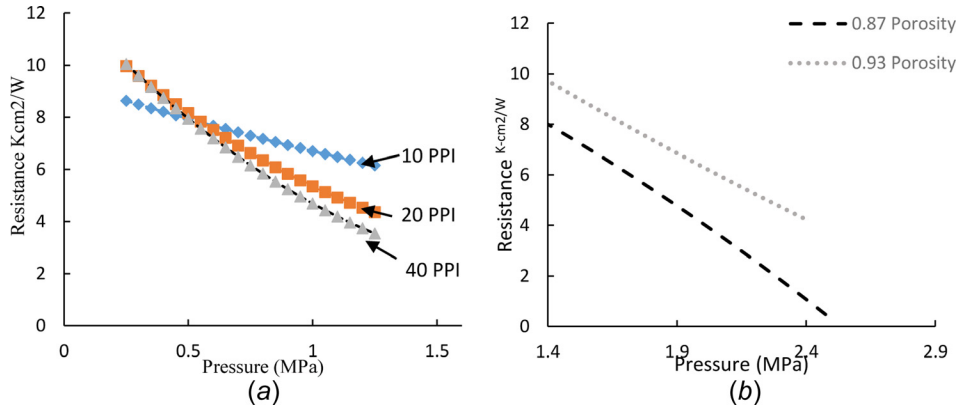
Fig. 12 (*a*) Contact resistance as a function of pressure for 10, 20, and 40 PPI and (*b*) contact resistance for 0.87 and 0.93 porosity

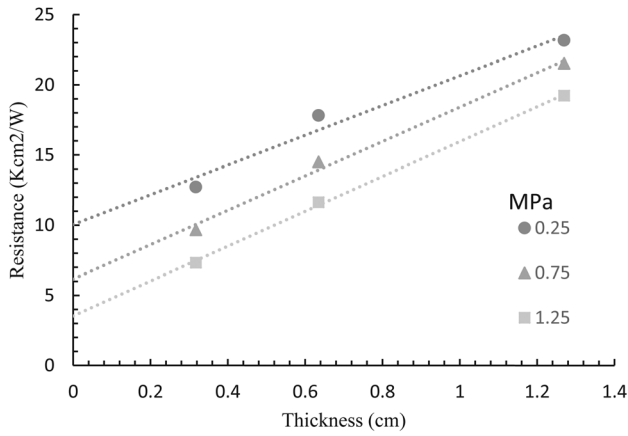$$R_{\text{tot}} = \frac{t}{k_{\text{eff}}} + 2R_{\text{cont}} \qquad (19)$$

Fig. 13 Thermal resistance extrapolation using multiple thicknesses for various pressures

6.1 Effect of Porosity. The experimental values for the total thermal resistances as a function of porosity are shown in Fig. 14. The samples with same pore size but varying porosity were chosen for this case. The results are plotted in variation of three thicknesses for specific porosity of 0.87, 0.93, and 0.95 in Figs. 14(*a*), 14(*b*), and 14(*c*), respectively, along with analytic model predictions. The analytic model predictions are simply an algebraic sum of the model used to calculate the contact resistance and intrinsic resistance (network analogy). For smaller porosity values between 0.87 and 0.93, the thermal resistance is larger for thicker sample in both cases. The 0.125 in. (3.175 mm) sample shows almost a linear trend with respect to increasing pressure. Whereas the 0.25 in. (6.35 mm) and 0.5 in. (12.7 mm) samples show asymptotic convergence to a specific value with increasing pressure. This is not observed for larger porosity samples, as shown in Fig. 14(*c*). The 0.5 in. thickness sample has a smaller thermal resistance than the thinner samples for higher loads. If only 0.5 in. thickness samples across different loads for multiple porosities are compared, we observe the smallest thermal resistance for the largest porosity among all the cases (Fig. 15). In Fig. 14(*c*), for higher porosity samples as all the curves merge together due to high deformation (since high porosity), the analytic
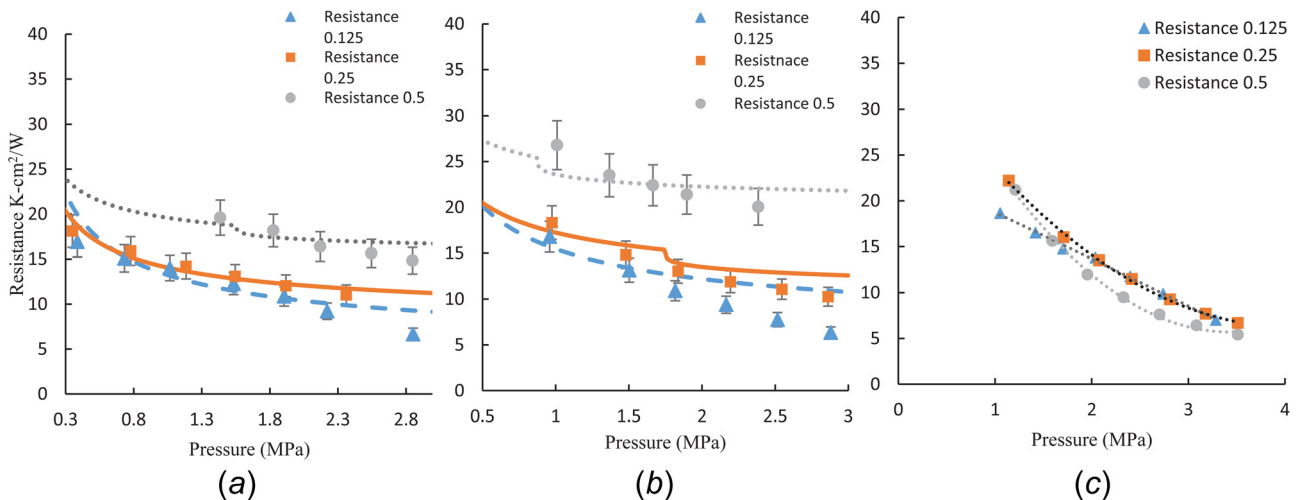

Fig. 14 (*a*) Experimental results for 0.87 porosity foams, (*b*) experimental results for 0.93 porosity foams, and (*c*) experimental results for 0.95 porosity foams
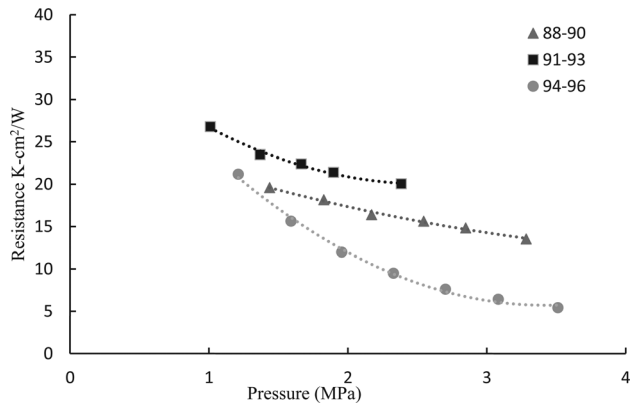
Fig. 15 Comparison of thermal resistance for various porosity ranges of 0.88–0.9, 0.91–0.93, and 0.94–0.96

Fig. 17 Repeatability data for 10 PPI, 0.25 in. 0.89 porosity samples

curve cannot come close to predicting these values. The rapid drop in the resistance corresponds to the second layer of the struts completely complying to come in contact with the opposing surface to increase the area of contact substantially and thereby decrease the contact resistance. The analytic model overpredicts the resistance at higher pressure values.

6.2 Effect of PPI. In case of variation of PPI of the samples, the results are plotted as a function of pressure for different thickness in Figs. 16(a)–16(c). Similar to the variation of porosity results, the thermal resistance is observed to drop inverse exponentially. As the pressure increases, the resistance is asymptotically converging to a constant value. Three distinct curves corresponding to three different thicknesses are observed in each case.

Repeatability of the experiments is summarized in Fig. 17. Experiments were carried out for four sets of samples with same specifications of porosity and pore size.

Additional experiments were carried out to check repeatability of results. Four samples with thickness 0.25 in., 10 PPI, and 0.88 porosity were tested under the same loading conditions, and the results were compared (Fig. 17). The expected variation in the measured thermal resistance was observed and corresponded to the measured uncertainty. The standard deviation found for an exponential regression was found to be 0.765 K cm^2/W.
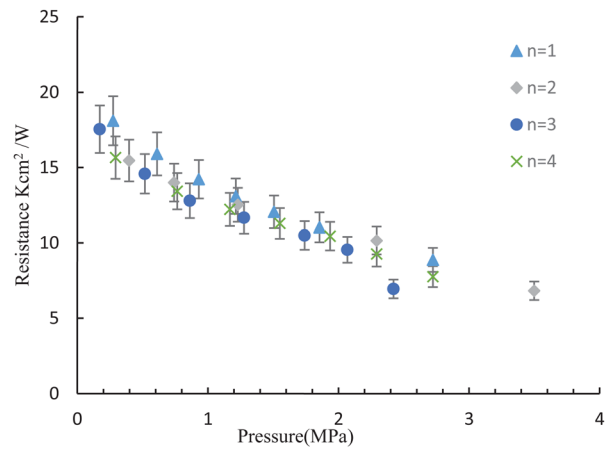
7 Discussion

We summarize the results data here along with analytic model and discuss the overall picture of the thermal resistance with respect to porosity and pore size.

The total thermal resistance values against the porosity show a drop in the thermal resistance for the high porosity samples (Fig. 18). This trend is more prominent at higher loads. The thermal resistance beyond the optimum point tends to increase up to unity porosity.

The experimentally observed trends hint toward existence of two competing effects that determine the total thermal resistance. These two effects are analogous to the length and width of the contact patch observed in the analytic models developed for the area of contact. As the length of deformation increases, the contact area will also increase, and consequently, the resistance will decrease. Beyond a point, the decreasing width of contact becomes a dominant factor, and hence as the porosity increases, the area of contact will reduce and the thermal resistance will become larger and larger. For larger porosity, multiple thermal resistance curves merge together as shown in Fig. 14(c), and the largest thickness sample actually shows a smaller thermal resistance. One of the reasons why this happens is that the effective Young's modulus becomes relatively small for larger porosity. As a result, the excessive deformation leads to better compliance
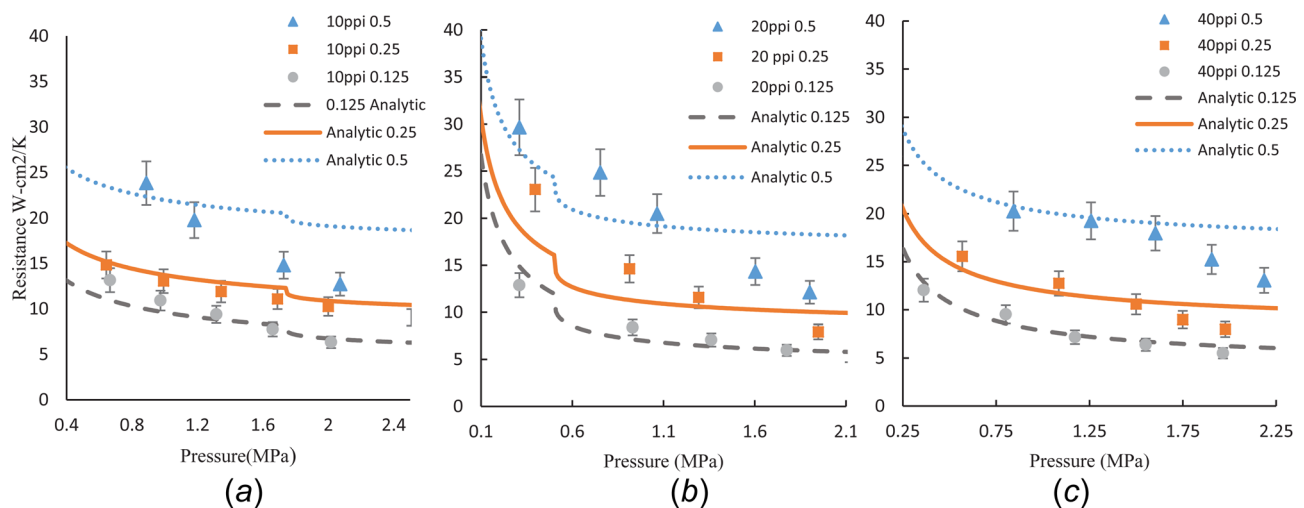

Fig. 16 (a) Thermal resistance for 10 PPI foams (0.89 porosity), (b) thermal resistance for 20 PPI foams (0.89 porosity), and (c) thermal resistance for 40 PPI foams (0.89 porosity)
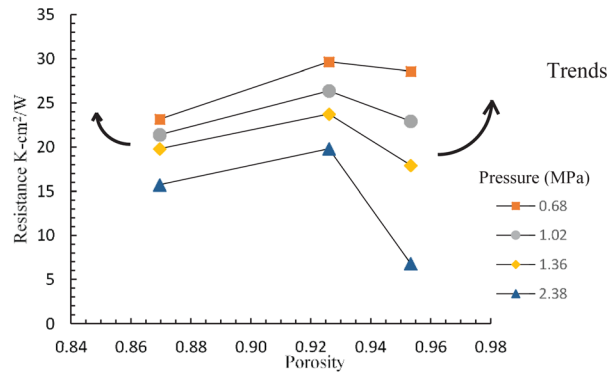
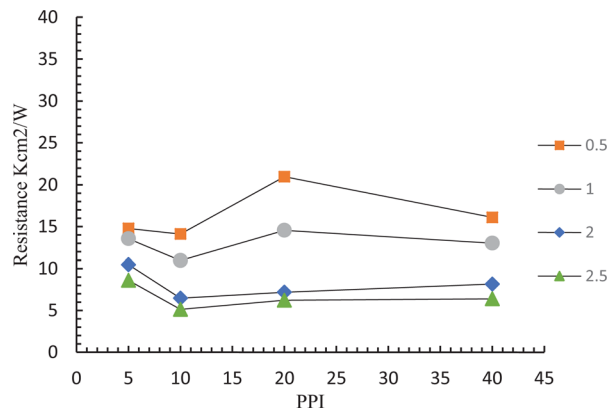**Fig. 18 Variation of thermal resistance against porosity for multiple pressures**

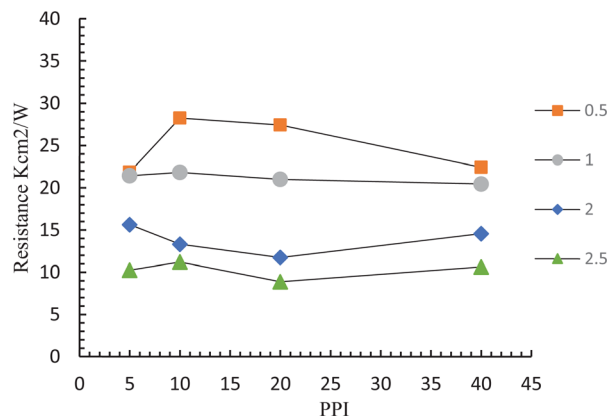**Fig. 19 Total resistance against PPI for 0.25 in. 0.89 porosity samples**

Fig. 20 Total resistance against PPI for 0.5 in. 0.89 porosity sample

against the rigid contacting surface. This implies that the contact resistance could be a function of the thickness of the sample. The thickness of the sample will directly influence the number of unit cell layers. The mechanical deformation characteristics and models for bulk properties consider the foam structure as a continuum, which requires existence of a minimum number of unit cells to be valid. This dependence of bulk properties and thereby the contact resistance on the thickness of the structures need to be investigated in further detail.

For the plot of thermal resistance against PPI, a drop in the resistance is observed at higher pressure (Figs. 19 and 20). There

is a tradeoff, however, with respect to variation of PPI. Larger PPI results in larger number of struts available for contact per unit area, but the radius of the struts is smaller for samples having same porosity. The effect of increasing number of struts is more dominant factor at higher pressures when all struts come in contact to the rigid opposing surface. This is the reason that we observe a drop in the thermal resistance at higher pressures, whereas at lower pressures, the same PPI results in a relatively higher thermal resistance.

The analytic models fail to predict the values of thermal resistance at very high porosity (>0.96) and large pore size (<10 PPI) since the model considers the deformation of the struts only in pure elastic mode. Additionally, the models deviate substantially for larger thickness sample. Possible reasons for limitations for higher porosity values could be attributed to three potential factors. First, internal buckling of struts occurring in the structure could affect the surface deformation characteristics. This would imply that the bulk properties of the foam could affect the thermal resistance indirectly by influencing the contact area. Additionally, there is a need of experimentation for characterizing effect of thickness on the contact resistance of the foam structure. Second, the model is limited to elastic deformations at the surface. Considering plastic yielding at contact could significantly affect the contact resistance at high porosity foams which have relatively thinner struts. Finally, a sensitivity analysis could provide insight on the effect of variation of contact regions across various samples on the effective thermal resistance of porous structures.

8 Conclusions

We developed a consolidated model considering both thermal and mechanical characteristic of the metal foam-based TIMs. Systematic study was done to determine the effective thermal conductivity as a function of geometric parameters of the foam. Numerical simulations and the developed analytic model provide close predictions of experimentally observed values following the ASTM D5470 standard for effective thermal conductivity.

Analytic model for microdeformation of the foams predicted an optimum value of porosity corresponding to the maximum area of contact. The generalized strut geometry incorporates any nonideal geometry manufactured. It also helps in engineering a custom structure that can have better compliance.

We experimentally investigated the total thermal resistance for various load and porosity conditions. The bulk resistance and contact resistance components were separately evaluated. The total thermal resistance decreases with increasing loads and approaches a constant value asymptotically. The trends for variation of thermal resistance with respect to porosity are coherent with what is observed in the analytic model. There is an optimum porosity which corresponds to maximum compliance and minimum thermal resistance close to 0.95. A minimum thermal resistance value of $5 \, K \, cm^2/W$ was found out for a 0.125 in. sample (10 PPI). As a future research, we will investigate composite materials filled in the pore space, which is will not only enhance the intrinsic thermal conductivity but also increase the total contact area. Currently, the model is limited to 0.88–0.95 porosity values and 5–40 PPI. The model could be extended to incorporate plastic deformations for evaluating surface contact. The applicability of model at high porosity and low PPI value could be addressed by investigating the effect of bulk properties and plastic deformation on the effective area of contact. Variation of thickness under pressure could also affect the bulk thermal resistance of the samples.

Research Center and an NSF Industry/University Cooperative Research Center at Purdue University.

Nomenclature

a = cube edge length (m)
A = area (m^2)
ap = apparent
d = dimensionless strut radius
e = dimensionless cube edge length
E = Young's modulus (Pa)
eff = effective
f = fluid
k = thermal conductivity (W/m K)
L = length of edge of TKDH (m)
n = number of struts in contact
p = ratio of cube length to pore radius
P = force (N)
r = radius of void sphere (m)
s = center-to-center distance between voids (m)
s = solid
t = total
w = width of contact area (m)
δ = deformation (m)
δ' = length of strut in contact (m)
ε = porosity

References

[1] Calmidi, V. V., and Mahajan, R. L., 1999, "The Effective Thermal Conductivity of High Porosity Fibrous Metal Foams," ASME J. Heat Transfer, **121**(2), pp. 466–471.

[2] Bhattacharya, A., Calmidi, V. V., and Mahajan, R. L., 2002, "Thermophysical Properties of High Porosity Metal Foams," Int. J. Heat Mass Transfer, **45**(5), pp. 1017–1031.

[3] Prasher, R., 2006, "Thermal Interface Materials: Historical Perspective, Status, and Future Directions," Proc. IEEE, **94**(8), pp. 1571–1586.

[4] Klett, J. W., Rommie, H., Romine, E., Walls, C., and Burchell, T. D., 2000, "High-Thermal-Conductivity, Mesophase-Pitch-Derived Carbon Foams: Effect of Precursor on Structure and Properties," Carbon, **38**(7), pp. 953–973.

[5] Chen, Z., Ren, W., Gao, L., Liu, B., Pei, S., and Cheng, H.-M., 2011, "Three-Dimensional Flexible and Conductive Interconnected Graphene Networks Grown by Chemical Vapour Deposition," Nat. Mater., **10**(6), pp. 424–428.

[6] Pettes, M. T., Ji, H., Ruoff, R. S., and Shi, L., 2012, "Thermal Transport in Three-Dimensional Foam Architectures of Few-Layer Graphene and Ultrathin Graphite," Nano Lett., **12**(6), pp. 2959–2964.

[7] Krishnan, S., Murthy, J. Y., and Garimella, S. V., 2006, "Direct Simulation of Transport in Open-Cell Metal Foam," ASME J. Heat Transfer, **128**(8), pp. 793–799.

[8] Doermann, D., and Sacadura, J. F., 1996, "Heat Transfer in Open Cell Foam Insulation," ASME J. Heat Transfer, **118**(1), pp. 88–93.

[9] Bauer, T. H., 1993, "A General Analytical Approach Toward the Thermal Conductivity of Porous Media," Int. J. Heat Mass Transfer, **36**(17), pp. 4181–4191.

[10] Boomsma, K., and Poulikakos, D., 2001, "On the Effective Thermal Conductivity of a Three Dimensionally Structured Fluid-Saturated Metal Foam," Int. J. Heat Mass Transfer, **44**(4), pp. 827–836.

[11] Dai, Z., Nawaz, K., Park, Y. G., Bock, J., and Jacobi, A. M., 2010, "Correcting and Extending the Boomsma–Poulikakos Effective Thermal Conductivity Model for Three-Dimensional, Fluid-Saturated Metal Foams," Int. Commun. Heat Mass Transfer, **37**(6), pp. 575–580.

[12] Paek, J. W., Kang, B. H., Kim, S. Y., and Hyun, J. M., 2000, "Effective Thermal Conductivity and Permeability of Aluminum Foam Materials," Int. J. Thermophys., **21**(2), pp. 453–464.

[13] Singh, R., and Kasana, H. S., 2004, "Computational Aspects of Effective Thermal Conductivity of Highly Porous Metal Foams," Appl. Therm. Eng., **24**(13), pp. 1841–1849.

[14] Leong, K. C., and Li, H. Y., 2011, "Theoretical Study of the Effective Thermal Conductivity of Graphite Foam Based on a Unit Cell Model," Int. J. Heat Mass Transfer, **54**(25), pp. 5491–5496.

[15] Wang, M., and Pan, N., 2008, "Modeling and Prediction of the Effective Thermal Conductivity of Random Open-Cell Porous Foams," Int. J. Heat Mass Transfer, **51**(5), pp. 1325–1331.

[16] Dukhan, N., Quiñones-Ramos, P. D., Cruz-Ruiz, E., Vélez-Reyes, M., and Scott, E. P., 2005, "One-Dimensional Heat Transfer Analysis in Open-Cell 10-ppi Metal Foam," Int. J. Heat Mass Transfer, **48**(25), pp. 5112–5120.

[17] Druma, A. M., Alam, M. K., and Druma, C., 2004, "Analysis of Thermal Conduction in Carbon Foams," Int. J. Therm. Sci., **43**(7), pp. 689–695.

[18] Maruyama, B., Spowart, J. E., Hooper, D. J., Mullens, H. M., Druma, A. M., Druma, C., and Alam, M. K., 2006, "A New Technique for Obtaining Three-Dimensional Structures in Pitch-Based Carbon Foams," Scr. Mater., **54**(9), pp. 1709–1713.

[19] Lemlich, R., 1978, "A Theory for the Limiting Conductivity of Polyhedral Foam at Low Density," J. Colloid Interface Sci., **64**(1), pp. 107–110.

[20] Negus, K. J., Yovanovich, M. M., and Beck, J. V., 1989, "On the Nondimensionalization of Constriction Resistance for Semi-Infinite Heat Flux Tubes," ASME J. Heat Transfer, **111**(3), pp. 804–807.

[21] Ma, Y., Yu, B., Zhang, D., and Zou, M., 2003, "A Self-Similarity Model for Effective Thermal Conductivity of Porous Media," J. Phys. D: Appl. Phys., **36**(17), p. 2157.

[22] Gibson, L. J., and Ashby, M. F., 1999, Cellular Solids: Structure and Properties, Cambridge University Press, Cambridge, UK.

[23] Kwon, Y. W., Cooke, R. E., and Park, C., 2003, "Representative Unit-Cell Models for Open-Cell Metal Foams With or Without Elastic Filler," Mater. Sci. Eng. A, **343**(1), pp. 63–70.

[24] Wicklein, M., and Thoma, K., 2005, "Numerical Investigations of the Elastic and Plastic Behavior of an Open-Cell Aluminium Foam," Mater. Sci. Eng. A, **397**(1), pp. 391–399.

[25] Zhu, H. X., Knott, J. F., and Mills, N. J., 1997, "Analysis of the Elastic Properties of Open-Cell Foams With Tetrakaidecahedral Cells," J. Mech. Phys. Solids, **45**(3), pp. 319–343.

[26] Sullivan, R. M., Ghosn, L. J., and Lerch, B. A., 2008, "A General Tetrakaidecahedron Model for Open-Celled Foams," Int. J. Solids Struct., **45**(6), pp. 1754–1765.

[27] Simone, A. E., and Gibson, L. J., 1998, "Effects of Solid Distribution on the Stiffness and Strength of Metallic Foams," Acta Mater., **46**(6), pp. 2139–2150.

[28] Phelan, R., Weaire, D., and Brakke, K., 1995, "Computation of Equilibrium Foam Structures Using the Surface Evolver," Exp. Math., **4**(3), pp. 181–192.

[29] Johnson, K. L., 1987, Contact Mechanics, Cambridge University Press, Cambridge, UK.